Analytica Chimica Acta 1212 (2022) 339892

Contents lists available at ScienceDirect

Analytica Chimica Acta

journal homepage: www.elsevier.com/locate/aca

Silver-fluoropolymer (Ag-CF_X) films: Kinetic study of silver release, and spectroscopic-microscopic insight into the inhibition of *P. fluorescens* biofilm formation

Giada Caniglia [a,1], Maria Chiara Sportelli [b,c,1], Anna Heinzmann [a], Rosaria A. Picca [b], Antonio Valentini [d], Holger Barth [e], Boris Mizaikoff [a], Nicola Cioffi [b,f,**], Christine Kranz [a,*]

[a] Institute of Analytical and Bioanalytical Chemistry, Ulm University, Albert Einstein Allee, 11, 89081, Ulm, Germany
[b] Chemistry Department, University of Bari "Aldo Moro", V. Orabona, 4, 70126, Bari, Italy
[c] CNR, Istituto di Fotonica e Nanotecnologie UOS Bari, Physics Department, Via Amendola, 173, 70126, Bari, Italy
[d] Physics Department, University of Bari "Aldo Moro", V. Orabona, 4, 70126, Bari, Italy
[e] Institute of Pharmacology and Toxicology, University of Ulm Medical Center, Albert Einstein Allee, 11, 89081, Ulm, Germany
[f] CSGI Consortium, Bari Unit, University of Bari "Aldo Moro", V. Orabona, 4, 70126, Bari, Italy

HIGHLIGHTS

- SECM measurement of Ag(I) release at fluoropolymer (Ag-CF_X) films.
- Correlation of release kinetics and swelling of films.
- Antimicrobial effect of the Ag-CF_X surfaces against *Pseudomonas fluorescens*.
- Long-term ATR-IR spectroscopy studies of biofilm formation.

ARTICLE INFO

Keywords:
Biofilm inhibition
Silver nanoparticles
Scanning electrochemical microscopy
Release kinetics
Korsmeyer-peppas model
Infrared attenuated total reflection spectroscopy

ABSTRACT

Silver-fluoropolymer (Ag-CF_X) composed of encapsulated bioactive nanophases within a thin polymer coating are promising antimicrobial films with excellent bioactivity. In this contribution, we report on Ag-CF_X thin films obtained by ion beam co-sputtering, accurately tuning film thickness, and inorganic loading. The Ag-CF_X films were characterized by spectroscopic and scanning probe microscopy techniques with respect to composition and swelling behavior. Next to electrothermal atomic absorption spectroscopy (ETAAS) studies, scanning electrochemical microscopy (SECM) experiments in combination with anodic stripping voltammetry (ASV) were carried out to study the release mechanism of silver(I) from the embedded silver nanoparticles (AgNPs). Silver(I) concentration profiles at the Ag-CF_X films in contact with water resulted in a release of 1310 ± 50 μg L^{-1} (n = 3) after 27 h of immersion and corresponded well to the swelling of the films. The antimicrobial properties towards biofilm formation of *P. fluorescens* were studied by attenuated total reflection Fourier-transform infrared (ATR-FTIR) spectroscopy during a period of 48 h. The obtained IR data revealed biofilm inhibition due to the presence of the antimicrobial layer but also indicated potential surface re-colonization after 30 h of contact with the bacteria-containing solution. The occurrence of cyclic changes in the characteristic IR bands correlated with apparent stress of bottom-layered bacteria, along with re-colonization on top of dead biomass, indicative of potential cannibalism events.

* Corresponding author.
** Corresponding author.
E-mail addresses: nicola.cioffi@uniba.it (N. Cioffi), christine.kranz@uni-ulm.de (C. Kranz).
[1] These Authors contributed equally.

https://doi.org/10.1016/j.aca.2022.339892
Received 26 November 2021; Received in revised form 19 April 2022; Accepted 28 April 2022
Available online 5 May 2022

1. Introduction

Bacterial biofilms represent a major cause of serious health issues in human medicine and the food industry, due to their ensuing resistance against harsh conditions and pharmacological treatments, in comparison with their planktonic counterparts [1]. Biofilms are defined as well-organized three-dimensional structures comprising cells rooted in a viscous matrix build-up by extracellular polymeric substances (EPS) [2]. This intricate system, mainly composed of polysaccharides, nucleic acids, and proteins, is dynamic, and its structure is strongly influenced by a plethora of parameters such as biofilm age and exterior conditions, e.g. nutrients deficiency, and attack of different agents [3]. The formation of biofilms is a complex multi-stage process, in which bacteria transmute from planktonic to sessile form. The interaction between bacteria in a biofilm and the surrounding environment can largely determine the extent and the composition of the bacterial colonies [4]. Depending on the stress conditions to which biofilms are exposed (e.g. the presence of antimicrobial agents), bacterial colonies can activate different survival strategies [5,6] including a cannibalistic response that may occasionally occur [7]. This behavior involves the secretion of cannibalism toxins, which favor the damage and death of bacteria from the same colony and the generation of lysed cells acting as nutrients. Methodologies for the investigation of biofilm formation have been developed or adapted to gain a comprehensive understanding of biofilm physiology, structure, and composition to find novel and more effective eradication strategies [8–10]. Biofilm growth may occur during extended timespans [11]; therefore, not only long-term effective bacterial treatments are required, but also appropriate analytical methods to study the long-term behavior of biofilms. Among others, attenuated total reflection Fourier-transform infrared (ATR-FTIR) spectroscopy is a powerful technique that provides *in-situ* and real-time monitoring of biofilm lifecycles with molecularly specific details on the first attachment stages [12,13].

Within the last decades, novel strategies to prevent biofilm growth have been developed and, among others, antimicrobials based on nanoparticles (NPs), such as ZnONPs, AgNPs, and CuNPs [14–16], have been intensively studied. Despite the numerous and strong antibiotics, which are nowadays available, infections caused by antimicrobial resistant bacteria are still a major cause of morbidity and mortality. Consequently, novel antimicrobial such as nanoparticle-based antimicrobial agents have been developed – among those - antimicrobial NPs and nanosized carriers for antibiotics delivery, which have shown high effectiveness for treating infectious diseases, including antibiotic resistant ones [15]. In comparison to ZnONPs and CuNPs, AgNPs have the capability to adsorb onto bacterial membrane, causing "pits" in the cell wall and consequent apoptosis. Moreover, AgNPs may induce the production of reactive oxygen species (ROS), causing oxidative stress to bacteria [17].

The controlled disposal of antimicrobial agents has been used as a strategy to release active species at specific rates to attenuate the formation of biofilms. The diffusion and migration processes of antimicrobials from NPs embedded in polymers are one of the principal strategies to achieve controlled release. In recent studies, AgNPs embedded in a fluoropolymer matrix (Ag-CF_X) have shown attractive properties as biocompatible antimicrobials with a controlled release of silver(I) ions [16,18–20]. It is known that AgNP-based films exhibit high antimicrobial properties, as silver(I) ions can damage the cell membrane, penetrate the cell, and induce oxidative stress via the generation of ROS [21]. The characterization of the antimicrobial films in respect with the release kinetics of silver(I) ions is therefore important to understand the efficiency of the antimicrobial films against biofilm formation. Herein, the kinetics of the silver(I) release has been studied using scanning electrochemical microscopy (SECM) and electrothermal atomic absorption spectroscopy (ETAAS). SECM is an *in-situ* scanning probe microscopy technique [22,23] that utilizes a micro- or nanoelectrode to obtain laterally resolved information on electrochemical properties of the investigated sample, such as heterogeneity of electron transfer kinetics [24,25] but also allows localized quantitative electroanalysis [26,27]. SECM has been used to investigate the electrochemical behavior of NPs-modified polymers in respect with the kinetic of silver (I) release and the AgNP distribution [28,29]. For example, in combination with voltammetric techniques, such as anodic stripping voltammetry (ASV), quantification of soluble electroactive species at sub-micromolar levels has been achieved [30].

Following previous studies performed by our research group on the antimicrobial properties of Ag-CF_X thin films [20], we investigate here the antimicrobial effectiveness of Ag-CF_X composites against *Pseudomonas fluorescens* biofilms. The amount of silver(I) release could be determined via SECM and ETAAS and was correlated to the effects on the surface colonization, with the eradication of the bacterial biofilm within few hours. The long-term ionic release properties of Ag-CF_X thin films, and their effect on mature *P. fluorescens* biofilms have been studied, correlating ionic release results with biofilm chemical response to the presence of the antimicrobial material. It should be pointed out that long-term surface/biofilm interactions pave the way for the possible evolution of antimicrobial resistance processes; for the first time, we provide here analytical insights in the events occurring during long-term interactions. ATR-IR data reveal that bacterial cells can re-colonize on dead biomass.

2. Material and methods

2.1. Ion beam sputtering deposition of Ag-CF_X thin films

Deposition of silver-fluoropolymer composite thin films is already described elsewhere [20]. Briefly, Ag-CF_X nanocomposites were deposited on silicon substrates (SiMat Silicon Materials, <110>, 300 μm, undoped, single-side polished) by co-sputtering a PTFE target (Good-Fellow LTD) and a pure silver target (Gambetti-CERAC, 99.999%) with Ar^+ beams, at room temperature and a pressure of 10^{-2} Pa. The silver volume fraction was $\varphi = 0.25$.

2.2. Characterization of Ag-CF_X films

Details on transmission electron microscopy (TEM) and atomic force microscopy (AFM) morphological characterization of Ag-CF_X are reported elsewhere [20,31]. TEM analysis was performed with a FEI (Eindhoven, The Netherlands) Tecnai T12 instrument and AFM measurements were obtained in contact mode using a Keysight Model 5500 AFM system (Keysight Technologies, AZ, USA). X-ray photoelectron spectroscopy (XPS) measurements were performed using a PHI (Chanhassen, MN, USA) Versaprobe II spectrometer, with monochromatized Al-Kα radiation (1486.6 eV). Experimental details and data treatment protocols for elemental analysis and peak fitting are described in Ref. [32]. The binding energy (BE) scale was calibrated taking the C1s spectrum at BE = 291.8 eV (–CF_2– component) as reference.

2.3. Study of silver(I) release kinetics

2.3.1. Electrothermal atomic absorption spectroscopy (ETAAS)

Spectroscopic quantification of the silver(I) released into an aqueous solution was performed using ETAAS. The Ag-CF_X samples were placed in contact with 500 μL of phosphate buffer saline solution (pH = 6.8, I = 0.1, Sigma Aldrich, Trace-SELECT®, for trace analysis, ≥99.999%, anhydrous) up to 48 h. 50-μL aliquots were analyzed after a dilution with 0.2% HNO_3 (Sigma Aldrich, 65–71%, Trace-SELECT® Ultra, for ultra-trace analysis), with a Perkin-Elmer PinnAAcle AS 900Z double-beam spectrometer (Milan, Italy). Further details on instrument calibration and data analysis can be found elsewhere [20]. Data analysis and processing was performed by OriginPro® 2016 softwareV 9.3 (Origin Lab Corporation).

2.3.2. Scanning electrochemical microscopy (SECM)

Electrochemical experiments were performed with a CHI842B potentiostat (CH Instruments, Austin, TX, USA) in combination with a three-electrode set-up using a platinum (Pt) counter (CE) and Ag/AgCl/KCl (sat.) reference (RE) electrode, respectively. A Pt disk ultramicroelectrode (UME) with a nominal radius of 12.5 μm was used as the working electrode (WE). Pt UMEs were fabricated according to well-established procedures [33], sealing a 12.5 μm radius Pt wire (Goodfellow, Bad Nauheim, Germany) in a borosilicate glass capillary (Hilgenberg GmbH, Massfeld, Germany). UMEs with RG ratios (*i.e.*, the ratio between the radius of the glass and the radius of the platinum wire) in the range of 10–12 were characterized by cyclic voltammetry in 1 mM ferrocene methanol/0.1 M KCl. Anodic square wave voltammetry (ASWV) was used to determine the concentration of the released silver (I) ions over time. A pre-concentration step of 120 s at −0.2 V *vs* Ag/AgCl/KCl (sat) was employed to deposit silver(I) onto the UME surface. The stripping ASWV was performed at 0.05 V s^{-1} scan rate, frequency of 25 Hz, 2 mV increments, and 25 mV amplitude. The concentration of the silver(I) ions was obtained from the area of the peaks in the potential range of −0.2 to 0.9 V. The limit of the detection (LOD) and limit of quantification (LOQ) were calculated based on the standard deviation of the response (S_y) of the calibration curve and the slope (S), according to: $LOD = 3(S_y/S)$ and $LOQ = 10(S_y/S)$. All experiments were performed at a tip-substrate distance equal to 79 μm, previously determined by using feedback mode approach curves, employing oxygen as electroactive species. Prior to the silver(I) release studies at the Ag-CF_X samples, calibration curves were recorded at the Pt UMEs in $AgNO_3$ standard solutions (stock solution 100 μM) using 0.1 M KNO_3 as electrolyte. $AgNO_3$ and KNO_3 were purchased from Merck (Germany), and all solutions were prepared in ultrapure water (18.0 MΩ cm, Elga Labwater; VWS Deutschland, Germany). Data evaluation was performed using Mira software (G. Wittstock, University Oldenburg, Oldenburg, Germany) and OriginPro® 2019b software, V 9.6.5.169 (Origin Lab Corporation).

2.4. Swelling measurements via atomic force microscopy

To perform swelling studies, Ag-CF_X samples were patterned using focused ion beam (FIB)-milling (DualBeam Helios Nanolab 600, ThermoFisher Scientific, Eindhoven, NL) with an acceleration voltage of 30.0 kV and a milling current of 0.3 nA. Swelling experiments were also carried out at mechanically removed films (scratches). These patterned Ag-CF_X samples were placed in the liquid cell of the AFM filled with ∼ 1.0 mL of MilliQ water or buffered solution and imaged at different immersion times at the same location. Images were acquired using a Keysight AFM system Model 5500 in contact mode AFM with a scan rate of 0.75 μm min^{-1} using a silicon nitride cantilever (ORC8 cantilever with 0.05 N m^{-1} nominal spring constant, Bruker). Data were processed using Pico Image Basic software, V 5.January 1, 5944 (Keysight Technologies).

2.5. Morphological characterization of biofilms on Ag-CF_X

Non-pathogenic *P. fluorescens* culture (DMS 50090) with an optical density (OD_{600}) equal to 1.6 was grown in 25 g L^{-1} Luria-Bertani broth. This bacteria suspension was then harvested and resuspended in a diluted LB medium (0.5 g L^{-1}) and seeded on Ag-CF_X films by immersing them into the bacteria solution and incubate the samples at 30 ± 1 °C, using a shaking incubator (KS 4000ic control, Keison Products, UK). After 40 h of incubation, the Ag-CF_X samples were rinsed twice with LB medium and MilliQ water. The samples were air-dried, and AFM images were recorded in air at room temperature in contact mode AFM (silicon nitride cantilever; nominal spring constant of 0.05 N m^{-1}). The bacteriall culture was incubated onto two different Ag-CF_X samples: an Ag-CF_X film prior to its exposure for 30 h to MilliQ water (swollen film) and a pristine Ag-CF_X sample. A statistical analysis of bacterial morphology variation has been performed using AFM images (20 × 20 μm^2) recorded in air in three different spots of the same sample. Statistical data evaluation was performed using ImageJ 1.53e software for the adjustment of the threshold and IBM SPSS Statistics V 27.0 (Armonk, NY: IBM Corp).

2.6. Monitoring of biofilm formation

2.6.1. Bacterial culture conditions

Non-pathogenic *P. fluorescens* cultures were prepared by inoculating 5 mL of 25 g L^{-1} sterile Luria–Bertani (LB) broth (dehydrated culture media, VWR International GmbH, Darmstadt, DE) at 27 ± 1 °C overnight, using a shaking incubator (KS 4000ic control, Keison Products, UK). The resulting bacterial suspension was harvested and re-suspended in 500 mL of LB medium (25 g L^{-1}) and incubated at 27 ± 1 °C up to a concentration of 10^8 CFU mL^{-1}. Bacterial growth was monitored by the OD_{600} using a UV-VIS spectrometer (Thermo Scientific NanoDrop One, Massachusetts, USA).

2.6.2. ZnSe ATR crystal modification

To evaluate the effectiveness of Ag-CF_X nanocomposites towards biofilm inhibition, ZnSe ATR crystals were modified with Ag-CF_X nanocomposites following two different strategies: by covering the entire surface of the crystal with the Ag-CF_X film and by the deposition of the film only onto the IR-inactive areas along the crystal surface (i.e., in between the internal reflections of the propagating IR radiation). Hence, the monitoring of the biofilm formation was investigated, by using (i) a fully surface-modified crystal, (ii) a partially modified crystal, and (iii) a pristine crystal, serving as a control specimen.

2.6.3. Characterization via ATR-FTIR spectroscopy

The experimental ATR-FTIR setup has been described elsewhere [20]. Briefly, the bacterial suspension of 10^8 CFU mL^{-1} in LB medium was pumped into the ATR-FTIR flow cell for 2 h, to favor the first attachment of bacteria at the ZnSe crystal. After 2 h, sterile LB medium (0.5 g L^{-1}) was pumped during 48 h and the development of the biofilm was monitored using a Bruker Tensor II Fourier transform infrared spectrometer (Bruker Optics GmbH, Ettlingen, DE). Changes of the amide II (1588–1483 cm^{-1}), amide III (1280–1196 cm^{-1}) bands, as well as the EPS (1187–952 cm^{-1}) and glycogen (1145 cm^{-1}) bands [20,34] were monitored for 48 h at 15 min intervals, recording spectra with a resolution of 4 cm^{-1} and an average of 128 scans for each spectrum. All interferograms were processed using the Mertz phase correction mode, and the Blackman-Harris three-term apodization function. Water vapor subtraction and baseline correction were applied on each spectrum. Data were processed for representation using OriginPro® 2016 software, V 9.3 (Origin Lab Corporation).

3. Results and discussion

3.1. Morphological and spectroscopic characterization of Ag-CF_X thin films

TEM and AFM data depicted in Fig. S1 show that the composite material, obtained by IBS deposition, is homogeneously distributed with a regular in-plane distribution of the AgNPs and an average NP size around 10 nm. Surface roughness and film thickness values are 1.48 ± 0.06 nm and 133 ± 11 nm (n = 3), respectively.

The chemical composition of the Ag-CF_X films was obtained by XPS and the elemental atomic percentages (Table S1) are in agreement with previous studies performed using a silver volume function (φ) equal to 0.25 with a surface Ag% equal to 4.5 ± 0.2. Ag photoelectron (Fig. S2a) and Auger (Fig. S2b) spectra were curve-fitted according to literature criteria [35] and led to an α' (modified Auger parameter) value of 724.0 ± 0.4 eV. The latter resulted to be in-between the value relevant to elemental Ag, and the one reported for Ag_2O [36,37]. This is reasonably due to a partial surface oxidation of the elemental Ag nanophases,

induced by air-exposure of the Ag-CF_X films.

Representative high-resolution XP spectra for the studied Ag-CF_X films are shown in Fig. S2. C1s signal (Fig. S2c) was fitted with six photoelectron components; that were attributed to the presence of alcoholic, carbonyl, and fluorinated unsaturated functional groups [20]. The F1s spectrum (Fig. S2d) shows a single component at 688.8 ± 0.3 eV (n = 3), which is univocally related to the organic fluorine [19] and confirms the absence of toxic inorganic fluorides.

3.2. SECM analysis

The quantification of the silver(I) was performed by combining SECM and ASWV (Fig. 1). The determination of silver(I) consists of two steps: firstly silver(I) is electrodeposited onto the UME surface and then (second step) stripped from the surface by the re-oxidation of the deposited silver, generating a current response, proportional to the concentration of silver(I).

To optimize the quantitative determination of silver(I), the redox behavior of silver(I) ions was investigated from the recorded calibration data. Depending on the concentration of the $AgNO_3$ solution, several anodic peaks were observed in the stripping step. Fig. 2 shows the representative square wave voltammograms at different silver(I) concentrations, from 210 μg L^{-1} to 2224 μg L^{-1}. In the range of 311–1300 μg L^{-1} (lower concentrations), two peaks are observed: a broad anodic peak at +0.56 V vs. Ag/AgCl and a well-defined anodic peak centered at +0.37 V vs. Ag/AgCl. A third sharp peak, correlated with concentrations of silver(I) higher than 1300 μg L^{-1}, appeared at +0.24 V vs. Ag/AgCl.

The electrochemical behavior of silver in neutral and weakly alkaline solutions has been extensively studied for decades, and the observation of the stripping anodic peaks in the potential window between −0.2 and +0.9 V vs. Ag/AgCl has been previously reported. Abduali et al. [38] describe the appearance of the peaks at +0.37 V and +0.56 V as a consequence of the formation of silver(I) oxide and silver(II) oxide, respectively, according to the following reactions:

$$2Ag + H_2O \rightarrow Ag_2O + 2H^+ + 2e^- \quad (3)$$

$$Ag_2O + H_2O \rightarrow 2AgO + 2H^+ + 2e^- \quad (4)$$

It is reported in the literature [39,40] that the peak at +0.24 V might be associated with the electro-dissolution of silver and the formation of the complex $[Ag(OH)_2]^-$:

$$Ag + 2OH^- \rightarrow [Ag(OH)_2]^- + e^- \quad (5)$$

Hampson et al. [40] showed that the stability of the dihydroxosilverate(I) in dilute alkaline solutions is due to an equilibrium between silver(I) oxide and silver(II) oxide. Hence, only the signals arising from the direct stripping of reduced silver species, i.e., the peaks at +0,37 V and +0.24 V vs. Ag/AgCl, result in a quantifiable response related to the actual silver(I) concentration. Fig. 3a and b show the peak deconvolution of a representative square wave voltammogram and the calibration

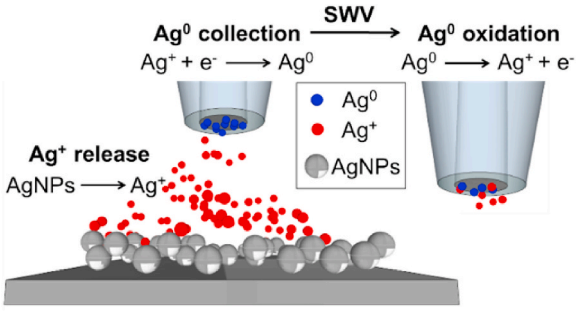

Fig. 1. Schematic showing the silver(I) release, deposition at the SECM tip and stripping.

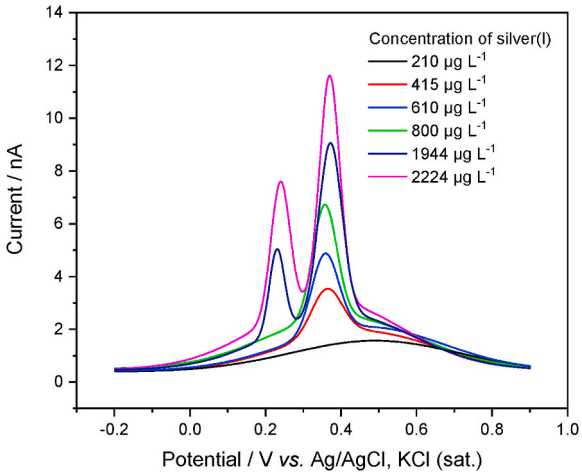

Fig. 2. Square wave voltammograms at different $AgNO_3$ concentrations measured in the bulk solution with a Pt UME (radius: 12.5 μm and RG = 9).

plot obtained from the sum of the integrated signal of the anodic current peaks at +0,37 V and +0.24 V, in a concentration range of 211–1947 μg L^{-1}. In this concentration range, a linear correlation was obtained (R^2 = 0.99112) and the obtained limit of detection (LOD) and quantification (LOQ) were determined with 74 μg L^{-1} and 245 μg L^{-1}, respectively.

3.2.1. Silver(I) release kinetics

In-situ information on the release kinetics of silver(I) species from the Ag-CF_X samples was obtained by combining SECM and ASWV measurements. The concentration of silver(I) was monitored as a function of time, after the UME was positioned at a distance of 79 μm above the surface. The UME to sample surface distance was determined by recording an approach curve above the Ag-CF_X surface (Fig. S3) using oxygen as redox active species [41]. Fig. S4 shows typical square wave voltammograms obtained for an Ag-CF_X sample during the first 27 h of immersion in 0.1 M KNO_3. The concentration of released silver(I) ions was evaluated by using the calibration curve recorded prior to the SECM experiments performed at the UME in a 0.1 M KNO_3 solution with known concentrations of $AgNO_3$. Fig. 4a shows the concentration profiles obtained within the first 27 h of contact of the Ag-CF_X films with the aqueous medium. A tendency to follow a pseudo-first order kinetic is clearly evident (R^2 = 0.98606), according to equation (6):

$$[Ag]_t = [Ag]_\infty (1 - e^{-kt}) \quad (6)$$

from which the values of the rate constant (k = 0.113 ± 0.008 h^{-1}) and the plateau concentration of released silver(I) ($[Ag]_\infty$ = 1310 ± 50 μg L^{-1}) could be extrapolated. The *in-situ* SECM-ASWV measurements were also compared with *ex-situ* ETAAS bulk experiments. Fig. 4b shows that the silver(I) release measured by ETAAS also follows a pseudo-first order kinetic (R^2 = 0.95265) with a release rate equal to 1.6 ± 0.7 h^{-1}, which reaches a plateau at 116 ± 7 μg L^{-1}. After 24 h, a further increase of the ionic release was detected, which revealed an almost linear correlation with time. This unexpected release was hypothesized to be related to substantial film swelling, which in case of extended contact with aqueous solutions activates a release mechanism that involves not only silver(I) species located at the thin film surface, but from the entire 3D volume of the film. Due to the hydrophobic nature of the Teflon-like matrix, as demonstrated in our previous studies [20], we believe that the penetration and subsequent swelling of the composite film is not immediate, after the addition of the aqueous solution; it becomes increasingly evident, with a sudden change at about 24 h, due to the depletion of the inorganic nanophases, leaving a more porous fluoropolymer structure, which is expected to be prone to 3D release mechanisms, in case of prolonged release and swelling experiments.

The significant difference in the silver(I) concentration between the

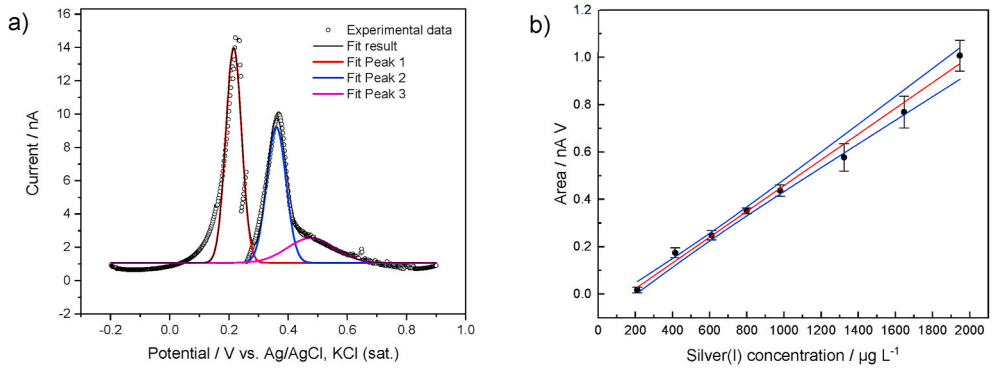

Fig. 3. (a) Peak deconvolution of an exemplary square wave voltammogram (silver(I) concentration in solution equals to 2735 µg L^{-1}). (b) Calibration curve (red line) of silver(I) recorded at a Pt UME with increasing $AgNO_3$ concentrations. The blue lines denote the uncertainty range, and the error bars reflect three repetitive measurements. Electrolyte: 0.5 M KNO_3. (For interpretation of the references to colour in this figure legend, the reader is referred to the Web version of this article.)

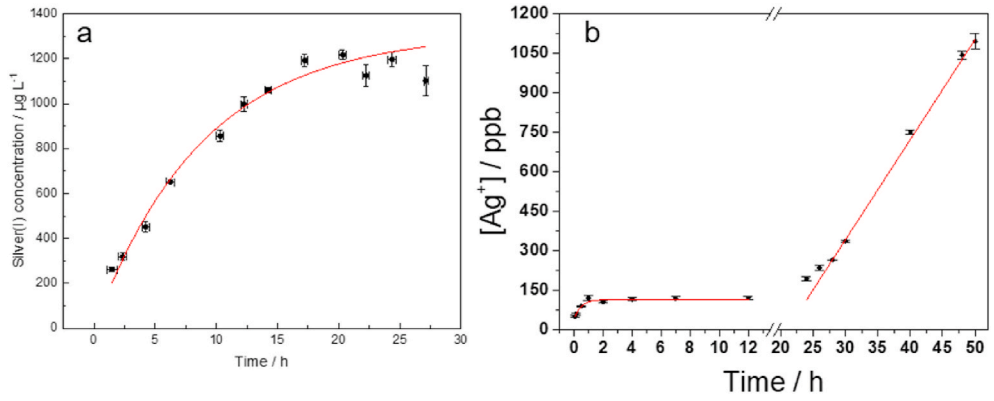

Fig. 4. (a) First-order kinetic model of silver(I) release obtained by SECM-ASWV at a distance of 79.0 µm above Ag-CF_X surface. (b) Long-term ionic release kinetics of Ag-CF_X thin film obtained by ETAAS. The error bars reflect the measurement of three different samples.

two experiments can be explained by the difference of the investigated area (bulk vs. localized) of each technique. In the case of the ETAAS measurements, as schematically depicted in Fig. 5a (estimated probed volume), the maximum concentration of released silver(I) after 24 h of immersion was around 116 µg L^{-1}, which is a weight of silver(I) equal to 0.058 µg in a volume of 500 µL. Considering that the contact area was π $(1)^2$ cm^{-2}, the total amount of silver(I) released per unit area was 0.0186 µg cm^{-2}. For the SECM experiments, the amount of silver(I) was calculated based on the electric charge of the stripping step. The charge was obtained from the anodic peak area of the voltammograms and, using Faraday's law (equation (7)), the amount of silver(I) was estimated as:

$$m = q\frac{M}{Fz} = \frac{Peak\ Area}{v}\frac{M}{F\,z} \tag{7}$$

Here, q is the electric charge in coulomb, M the atomic mass of silver in g mol^{-1}, F is the Faraday constant, z the valency of the ion, and v the stripping scan rate (0.05 V s^{-1}). The total amount of silver(I) was determined as 1.3 10^{-5} ± 0.1 10^{-5} µg (n = 3). The area of the sample investigated in the SECM experiment (Fig. 5b) can be roughly approximated to the total UME diameter (which equals the electroactive diameter and surrounding glass shielding). Considering an average radius of 145 µm, obtained by optical microscopy, the total area investigated was approx. 7.45·10^{-4} cm^2, thus the amount of silver per unit

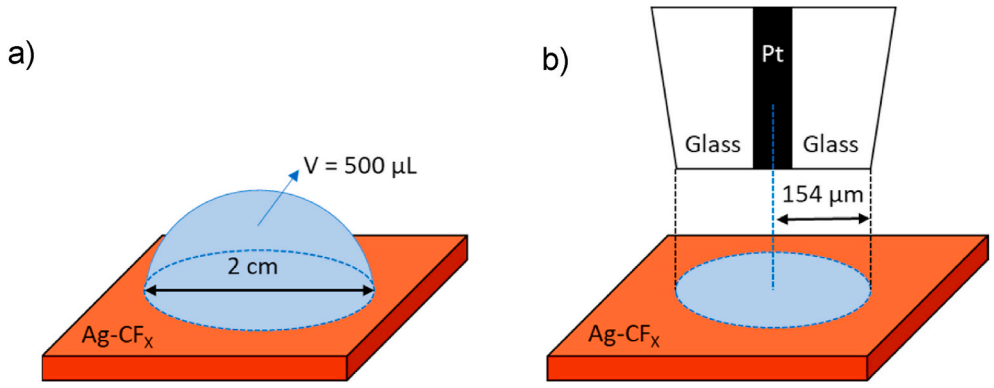

Fig. 5. (a) Schematics of the probed area by ETAAS. (b) Geometry of a SECM tip approached to the surface and the diffusion layer of silver(I).

area was 0.0174 μg cm^{-2}.

Hence, taking into account the amount of silver(I) released per unit area, the comparison of the performed experiments (SECM and ETAAS) revealed an excellent agreement with a relative error lower than 2.5%.

To investigate the kinetics of silver(I) release from the Ag-CF_X films, the data obtained for the first 14 h of immersion, were fitted to the Korsmeyer-Peppas model [42], which was developed to describe the drug release from polymeric substrates by combining Fickian and non-Fickian diffusion. Diffusion is, thus, controlled by the relaxation of the polymeric chains that is related to the diffusion of water into the polymer, yielding a swelling of the organic matrix [43]:

$$\frac{M_t}{M_{inf}} = kt^n \tag{8}$$

Here, M_t/M_{inf} is the fraction of drug released in time t, k is the kinetic rate constant and n is the release exponent, which describes the mechanism of the drug release.

Depending on the value of the n exponent, the drug release mechanism can be classified as case-I (Fickian model), case-II (non-Fickian model), and anomalous transport [44]. In case-I, the drug release is governed by thermodynamic forces, such as concentration and chemical potential gradients, and the solvent diffusion rate is higher than the processes related with the polymeric chain relaxation. Hence in case-I, the release is controlled only by diffusional processes of the drug. In contrast, in case-II transport the drug release is influenced by other physical-chemical processes, such as swelling and polymeric relaxation. The anomalous transport is an intermediate behavior between case-I and case-II in which the drug release is controlled by diffusion and swelling, i.e., the diffusion and the swelling rates are equivalent. In case, the geometry of the substrate is a slab or a thin film, such as the Ag-CF_X samples, the two limiting cases are the diffusion-controlled release (n = 0.5) and the swelling-controlled release (n = 1.0). Values between 0.5 and 1.0 describe the superposition of both limiting cases.

The log-log plot of $[Ag^+]_t/[Ag^+]_\infty$ versus time (Fig. 6) fits quite nicely to the Korsmeyer-Peppas model, according to the following equations:

$$\mathrm{Log}[Ag^+]_t = \mathrm{Log}[Ag^+]_\infty + \mathrm{Log(k)} + \mathrm{nLog(t)} \tag{9}$$

$$\mathrm{Log}\frac{[Ag^+]_t}{[Ag^+]_\infty} = \mathrm{Log(k)} + \mathrm{nLog(t)} \tag{10}$$

where $[Ag^+]_t$ is the concentration of silver(I) in time t and $[Ag^+]_\infty$ is the maximum amount of silver(I) released that was obtained by the study of the pseudo-first order kinetic. Under the experimental conditions, the rate constant was 0.1593 ± 0.0001 h^{-1} (n = 3) and the n value was 0.6420 ± 0.0003 (n = 3), suggesting that the silver(I) release was mainly controlled by the swelling of the Ag-CF_X matrix.

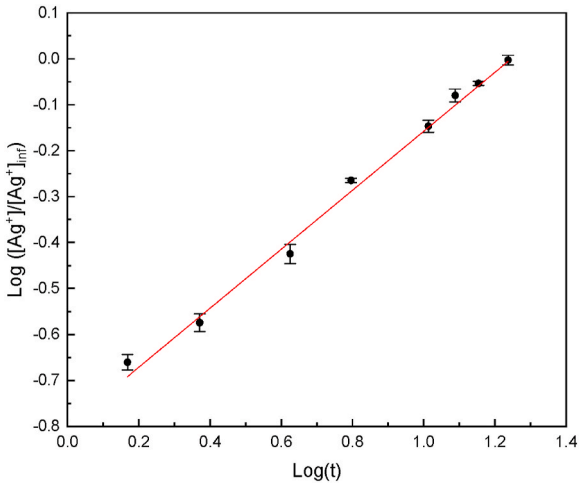

Fig. 6. vs. *log(t)* graph according to the Korsmeyer-Peppas kinetic model of silver(I) release at the distance of 79.0 μm above the Ag-CF_X surface. The error bars reflect the measurement at three different samples.

According to the literature [45–47], the inherent mechanism of silver (I) release from the fluoropolymer can be described by firstly diffusion of the water into the polymer matrix leading to subsequent swelling of the film and the oxidation of the Ag-NPs to silver(I) ions, which diffuse into the solution.

3.3. Swelling properties of the Ag-CF_X films

Fig. 7a and b show the AFM topography images of FIB-milled patterned and scratched Ag-CF_X samples recorded in air. The heights of the film were obtained via cross-sectional AFM line-scans (Fig. 7c and d) at the patterns/scratches. The swelling was calculated according to the following equation:

$$\mathrm{Swelling} = D_s - D_d \tag{11}$$

where D_s and D_d are the depths of the pattern/scratch in the swollen and the dry state, respectively.

As expected, the polymeric matrix shows swelling behavior when the film is in contact with MilliQ water resulting a total swelling of 128 ± 5 nm (n = 3) after 14 h of immersion, and at that time also a plateau is reached (Fig. 7e). Similar behavior was observed in buffered solution with a slightly reduced swelling behavior of approximately 30 nm (Fig. S5).

Fig. 7f presents the overlay of the swelling behavior of the FIB-modified (black dots) and the scratched samples (red dots). We are well aware that the impact of the Ga^+ ion beam on the polymer leads to increased crosslinking [48–51], which is also confirmed by XPS measurements (see Fig. S6). Interestingly, the altered crosslinking in the area of the FIB-patterns does not significantly affect the swelling behavior of the organic matrix within the first 14 h of immersion in MilliQ water, which is clearly visible in the overlaid data of the swelling behavior of films with the film mechanically removed and FIB-milled sample, as shown in Fig. 7f.

3.4. Investigation of P. fluorescens biofilms grown on Ag-CF_X thin films

To understand the antimicrobial effect due to the release of silver(I) from the Ag-CF_X films on the growth of biofilms, a culture of *P. fluorescens* in Luria Bertani broth (OD_{600} = 1.60) was incubated at 30 °C for 30 h on either a previously swollen Ag-CF_X surface or a pristine Ag-CF_X film. The swollen Ag-CF_X was prepared by immersing a pristine sample in MilliQ water for 30 h to trigger silver(I) release. AFM imaging was performed to investigate the density and morphology of bacteria and formed biofilm.

Fig. 8a and b shows AFM topography images of *P. fluorescens* after the incubation on the pristine Ag-CF_X film and the swollen film, respectively.

It is clearly evident that the density of bacteria in contact with the two different films (pristine and swollen) is significantly different. The swollen film, which is assumed to have a reduced surface atomic percentage of Ag due to the release of silver ions [20], shows a higher bacterial density and the formation of biofilm, as visible in Fig. 8b. The surface coverage was 41.5 ± 0.7% (n = 3) evaluating an area of 60 × 60 μm^2. Whereas at the pristine sample, where the silver(I) release took place during the incubation of the bacteria, results in a significant lower number of bacteria and attenuated formation of biofilm, with a coverage of 24.1 ± 0.5% (n = 3), as shown in Fig. 8b and c, respectively.

It is worth mentioning that after 30 h of incubation on a pristine Ag-CF_X sample, bacteria exhibit also different shapes. Fig. 9a shows that at the pristine sample, a layer of coccoid round-shaped bacteria are visible around of rod-shaped cells, while at the swollen film (Fig. 9c), the shape and size of the bacterial cells show the expected rod-shaped form, which

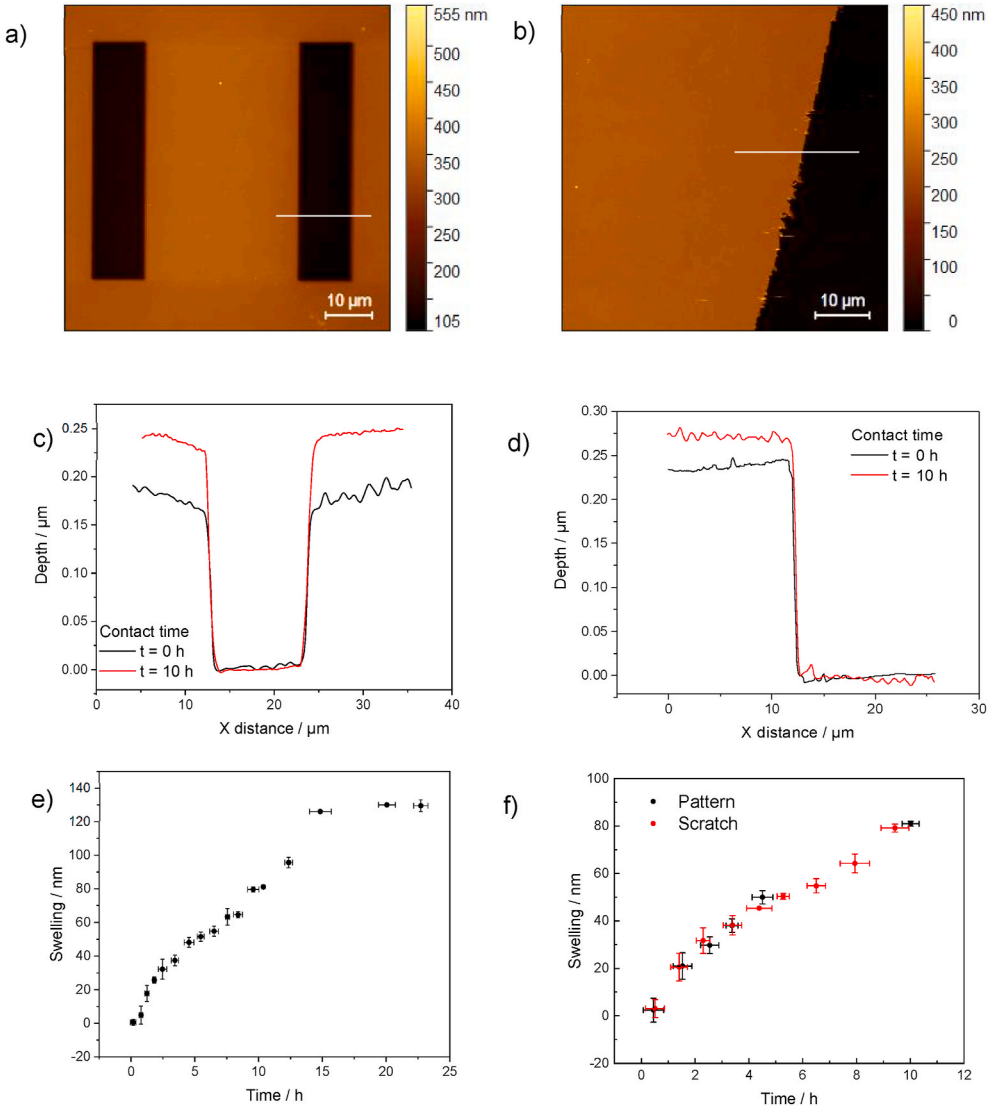

Fig. 7. AFM image in air of the (a) patterned Ag-CF_X film on silicon substrate and (b) scratched Ag-CF_X film on silicon substrate. (c) Cross-section displaying the depth profile of the patterned Ag-CF_X sample before the immersion in water and after 10 h of immersion. (d) Cross-section displaying the depth profile of the scratched Ag-CF_X sample after the immersion in water and after 10 h of immersion. (e) Swelling behavior of Ag-CF_X film monitored in water over a time of 24 h. (f) Swelling behavior of patterned (black) and scratched (red) Ag-CF_X sample in MilliQ water monitored for 10 h. The error bars reflect the measurement at three different samples. (For interpretation of the references to colour in this figure legend, the reader is referred to the Web version of this article.)

is the characteristic morphology of the *P. fluorescens* in the absence of antibacterial agents [52]. It is well known that as response to environmental stress, such as nutrients starvation, extreme pH conditions or the presence of antimicrobials, the morphology of bacteria may be altered. Cefali et al. [53] suggested that the change in morphology from rod-like to a smaller and coccoid shape can be associated with the reduced energy requirements to overcome hostile conditions. Hence, the presence of a layer of round-shaped cells may limit the adverse effects of silver(I) released from the Ag-CF_X film to a new layer of bacteria grown in a less hostile environment as indicated through the rod-like morphology of the bacteria.

The morphology of the bacteria was statistically evaluated in terms of circularity, from three AFM images (area: 20 × 20 µm^2) recorded at different locations of the same sample. Circularity ($\mathscr{C}$) is defined as the degree of roundness of an object and is calculated based on equation (12):

$$\mathscr{C} = 4\pi \frac{Area}{(Perimeter)^2} \tag{12}$$

Thus, values of circularity proximate to 1.0 describe typical coccoid-shaped cells (with a length to width ratio close to 1.0), while values of circularity below 0.7 are more characteristic of rod-shaped bacteria with length to width ratios higher than 2.4–2.5 [52].

ANOVA statistical tests (significance level $\alpha = 0.05$) show that there is not significant difference among the three AFM images recorded of each sample; thus, the pristine and the swollen samples can be assumed homogeneous. In order to compare the different morphology of the bacteria in the pristine and swollen samples, the non-parametric Mann-Whitney U test ($\alpha = 0.05$) was performed and it revealed that there is a statistical difference between the circularity, i.e., the morphology, of the bacteria grown in the pristine ($\mathscr{C} = 0.68 \pm 0.04$, n = 300) and in the swollen ($\mathscr{C} = 0.91 \pm 0.04$, n = 300) samples. Fig. 9b and d show the shape distribution of the bacteria in terms of circularity in the pristine and swollen samples, respectively.

3.5. Spectroscopic characterization of biofilms grown on Ag-CF_X thin films

In addition, a comprehensive ATR-FTIR study was performed to evaluate the effectiveness of Ag-CF_X nanocomposites towards biofilm inhibition. Amide I, amide II and EPS bands were monitored over time, as they are indicative of biofilm formation and proliferation [54]. ZnSe ATR crystals were modified with Ag-CF_X nanocomposites in a variety of ways. Firstly, only IR-inactive areas along the crystal surface (i.e., in between the internal reflections of the propagating IR radiation) were covered with the film, as already demonstrated during short-term IR biofilm inhibition studies [20]; subsequently, the entire crystal surface

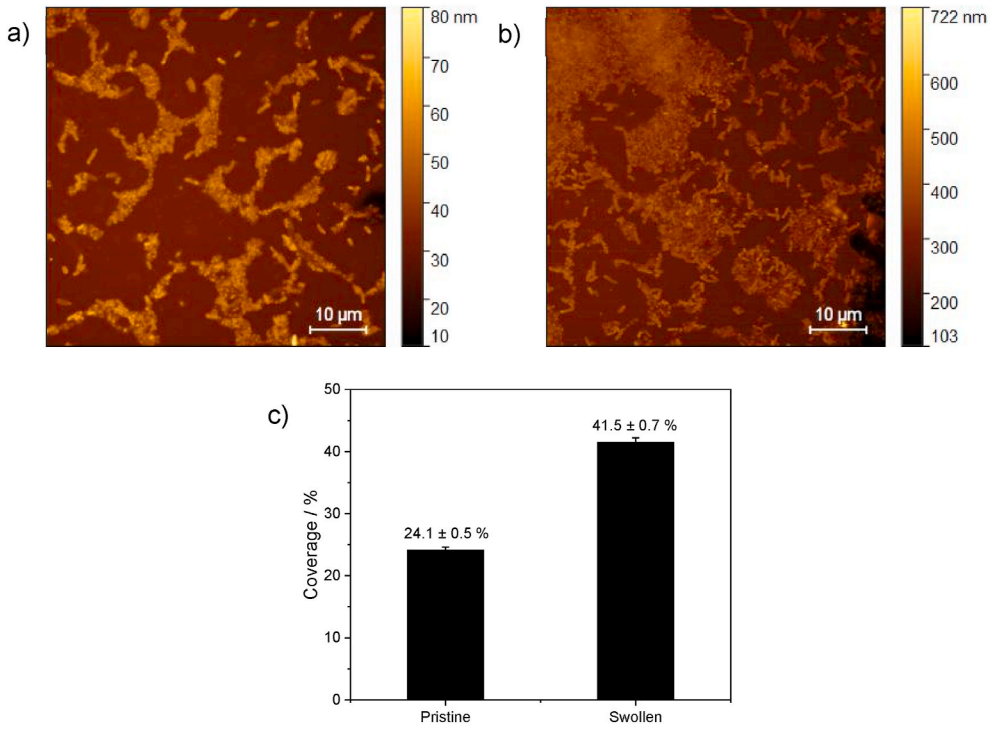

Fig. 8. Contact mode AFM topography image recorded in air of *P. fluorescens* after 30 h of incubation on the (a) pristine and (b) swollen surface Ag-CF_x. (c) Bar chart of the measured coverage (error bars reflect the measurements of three different samples).

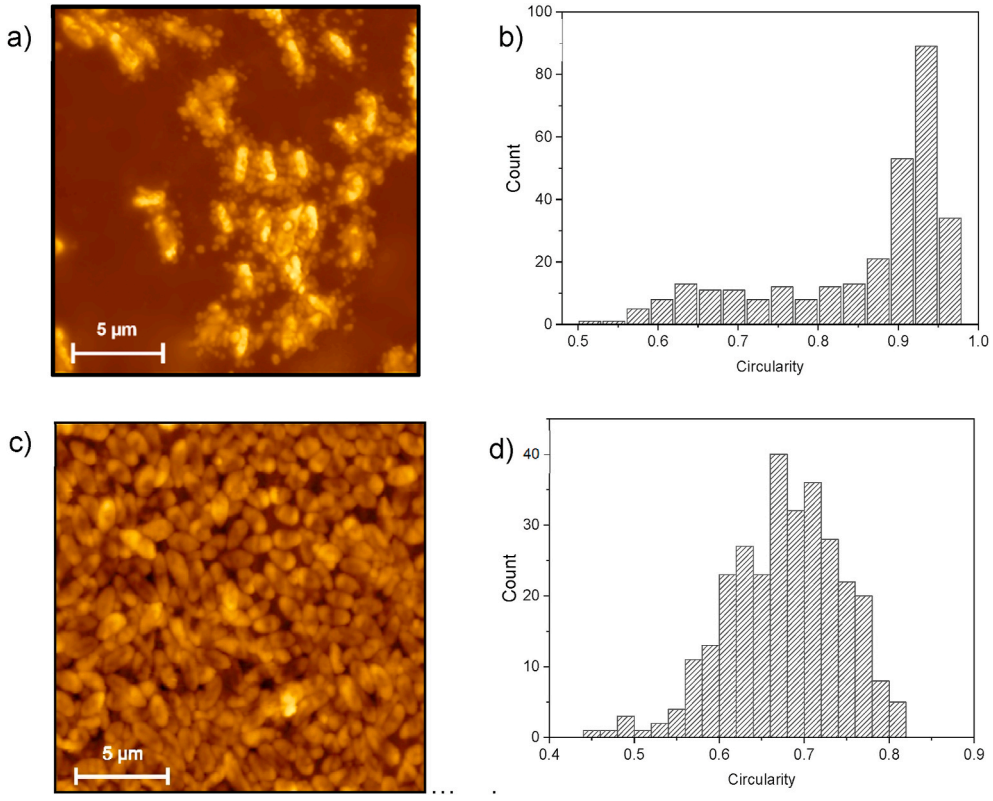

Fig. 9. (a) Contact mode AFM topography image of P. fluorescens after 30 h of incubation on a pristine sample and (b) frequency counts of bacteria circularity. (c) Contact mode AFM topography image of P. fluorescens after 30 h of incubation on a previously swollen film and (d) frequency counts of bacteria circularity. Images were recorded in air.

was modified with a 150-nm-thick film. Hence, three different experiments were carried out: (i) using fully surface-modified crystals (ii) partially modified (i.e., patterned) crystal surfaces, and (iii) control experiments using a bare crystal without antimicrobial thin film. All experiments were performed over a 48 h timespan at the same experimental conditions. Fig. 10 shows the time dependence of the band areas relevant to biofilm development. In the case of the bare crystal (Fig. 10a), all bands significantly increased as a function of time. After 30 h, the integrated peak areas of amide I and II almost reached a steady state, indicating a lower attachment of new bacteria to the biofilm and returning to grow rapidly after 40 h. These findings indicate that bacteria start to colonize on existing biomass after almost two days. This is consistent with findings of Humbert et al. [34] and Stenclova et al. [12], who observed a similar evolution of amide II and EPS characteristic bands resulting from bacterial (re-)colonization at the crystal surface after the maturation/detachment stages [12]. Presence of a thick biofilm, which exceeds the evanescent field, cannot be excluded [12].

Fig. 10b reveals the evolution of the same bands for a biofilm grown on a patterned crystal. In general, crystal colonization appeared to be slowed down by the presence of the antimicrobial coating. Instead, the EPS band grew faster showing a strong increase after 15 h and 30 h, respectively. This may be related to the attempt of recolonization of biofilm on top of dead biomass [34]. Fig. 10c describes the variation of band area as a function of time for a fully modified crystal. It is evident that there is no biofilm attachment at the crystal surface. This can be indicative of the fact that the Ag-CF_X thin film exerts not only an antibacterial action, but also shows an antifouling effect. Following these general observations, the spectra were evaluated in more detail studying the evolution of selected peaks of the three different experiments. In particular, the bands relevant to amide II (~1550 cm^{-1}), glycogen (~1145 cm^{-1}) and nucleic acid phosphate groups (~1220 cm^{-1}) were evaluated. It is known that a sharp decrease of Amide II band is associated with the removal of biofilm sections from the colonized surface [55] (Fig. 11a). This removal can be either due to the accumulation of an excessive amount of biomass at the colonized surface, or due to stress/starvation. The experiment using a bare crystal revealed that the band decreased after approx. 30 h, which could be related to an excessive accumulation of bacteria and to partial detachment of the biofilm [56]. For the patterned crystal, the intensity decreased after approx. 20 h, probably because of the stress induced by the antimicrobial material (for contact times >7 h, the silver(I) concentration in solution reached its maximum), and the band intensity returned to its initial level after 40 h indicating a possible re-colonization of the surface. No colonization was observed for the completely modified crystal. Regarding DNA and RNA phosphate groups (i.e., nucleic acids), an increase of the band associated to the asymmetric PO_2^- stretching vibration from DNA and RNA is an indication of the increase in metabolic activity of the biofilm [57] (Fig. 11b). For the bare crystal, metabolic activity was continuously increasing except a slight shift at approx. 10 h. For the patterned crystal, the intensity decreased after 20 h, because of stress induced by the antimicrobial film followed by a gradual increase during the remaining experiment. This is indicative of a likely re-colonization of the surface. Absence of colonization was confirmed for the completely modified crystal.

An additional comparison of the evolution of glycogen and amide II band was also performed, as shown in Fig. S7 and comments therein. As expected from the AFM experiments, images obtained by optical microscopy at the interface of the coated and the bare areas of the ZnSe crystal (Fig. S8) show similar round-shaped bacteria in the areas with the presence of the Ag-CF_X film, whereas predominantly rod-shaped bacteria are visible on the bare crystal.

4. Conclusions

This work demonstrates the efficiency of a second-generation antimicrobial nanomaterials based on Ag-NPs embedded in a fluoropolymer matrix (Ag-CF_X). The advantage of these films is a low toxicity which is evident based on the absence of potentially toxic inorganic fluorides, confirmed by XPS experiments. Silver(I) release from Ag-CF_X has been investigated using SECM in combination with ASWV. The results confirmed the inherent relation between the kinetic of the antimicrobial release with the swelling of the organic film, which could be confirmed by the Korsmeyer-Peppas mathematical model. We could show the antimicrobial effect of the Ag-CF_X surfaces against *Pseudomonas fluorescens* revealing the difference in density of the formed biofilm and the morphology of the bacteria for pristine and swollen Ag-CF_X films. According to the literature, bacteria exhibit a coccoid shape to counteract the effect of the presence of antimicrobial silver(I), while in an environment with an expected reduced concentration of antimicrobial (swollen films), bacteria grow without any change in the morphology. Also, the antimicrobial properties of the Ag-CF_X films were confirmed by long-term experiments (48 h) performed with ATR-FTIR spectroscopy. The absorption bands related to the amide I, amide II, EPS, and glycogen vibrations were investigated, and we could show that the silver(I) release can slow down surface colonization and enables the eradication of the bacterial biofilm within few hours. ATR-FTIR data also confirmed that bacterial cells can re-colonize on dead biomass when the latter is thick enough to prevent direct interaction with the antimicrobial surface. In other words, dead biomass in direct contact with the active coating may behave like a sink for ionic silver, lowering its availability in case of further bacterial colonization of the same surface. In conclusion, this study represents an excellent approach for investigating biofilm formation on antimicrobial surfaces over extended periods of time. It is a promising strategy to better understand the early stages that lead to the antimicrobial resistance phenomena.

CRediT authorship contribution statement

Giada Caniglia: Data curation, writing - review and editing. **Maria Chiara Sportelli:** Writing – review & editing. **Anna Heinzmann:** Data curation. **Rosaria A. Picca:** Formal analysis. **Antonio Valentini:** Data curation. **Holger Barth:** Supervision. **Boris Mizaikoff:** Supervision.

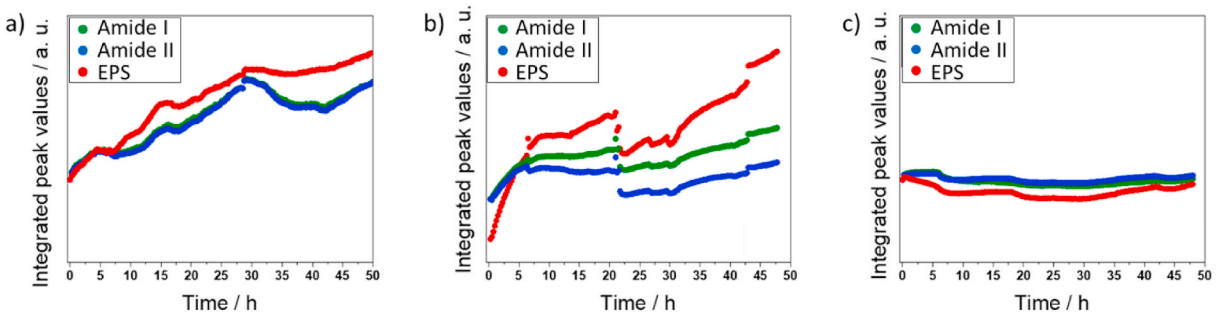

Fig. 10. Integrated peak values as a function of time obtained by ATR-FTIR monitoring of biofilm growth on a bare ATR crystal (a), on a patterned crystal (b), and on a fully covered crystal (c).

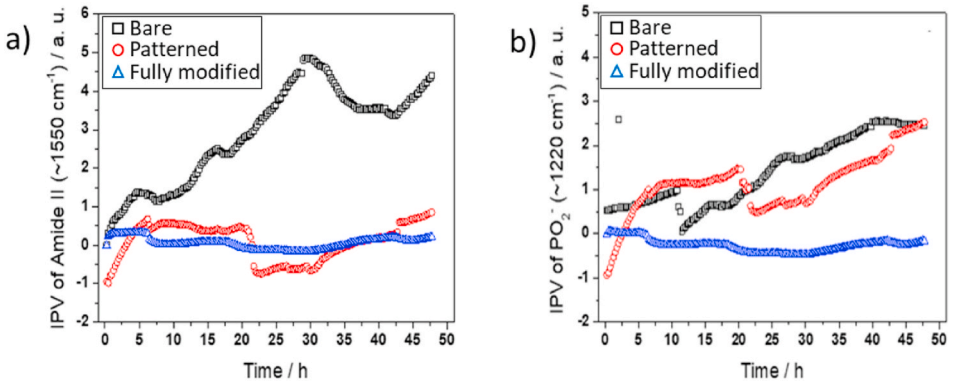

Fig. 11. (a) Integrated peak values for amide II band of biofilm growth; (b) integrated peak values for the ν_{as} PO_2^- band of biofilm growth. Data on a bare ATR crystal (black line), on a patterned crystal (red line), and on a fully covered crystal (blue line). (For interpretation of the references to colour in this figure legend, the reader is referred to the Web version of this article.)

Nicola Cioffi: Supervision - review and editing. **Christine Kranz:** Supervision, Writing – review & editing.

Declaration of competing interest

The authors declare that they have no known competing financial interests or personal relationships that could have appeared to influence the work reported in this paper.

Acknowledgements

This work is part of the "Break Biofilms" project that has received funding from the European Union's Horizon 2020 research and innovation program under the *Marie Skłodowska Curie* Grant Agreement No. 813439. M.C.S. acknowledges the financial support from Fondo Sociale Europeo "Research for Innovation (REFIN)"; project n° 435A866B. Dr. G. Neusser and the FIBCenter UUlm are acknowledged.

Appendix A. Supplementary data

Supplementary data to this article can be found online at https://doi.org/10.1016/j.aca.2022.339892.

References

[1] N. Billings, A. Birjiniuk, T.S. Samad, P.S. Doyle, K. Ribbeck, Material properties of biofilms—a review of methods for understanding permeability and mechanics, Rep. Prog. Phys. 78 (2015), 036601, https://doi.org/10.1088/0034-4885/78/3/036601.

[2] J.W. Costerton, Z. Lewandowski, D. DeBeer, D. Caldwell, D. Korber, G. James, Biofilms, the customized microniche, J. Bacteriol. 176 (1994) 2137–2142, https://doi.org/10.1128/JB.176.8.2137-2142.1994.

[3] D.O. Serra, A.M. Richter, G. Klauck, F. Mika, R. Hengge, Microanatomy at cellular resolution and spatial order of physiological differentiation in a bacterial biofilm, mBio 4 (2013) e00103–e00113, https://doi.org/10.1128/mBio.00103-13.

[4] V. Sihorkar, S.P. Vyas, Biofilm consortia on biomedical and biological surfaces: delivery and targeting strategies, Pharmaceut. Res. 18 (2001) 1247–1254, https://doi.org/10.1023/A:1013073508318.

[5] S. Yu, Q. Wei, T. Zhao, Y. Guo, L.Z. Ma, A survival strategy for Pseudomonas aeruginosa that uses exopolysaccharides to sequester and store iron to stimulate psl-dependent biofilm formation, Appl. Environ. Microbiol. 82 (2016) 6403–6413, https://doi.org/10.1128/AEM.01307-16.

[6] D.B. Roszak, R.R. Colwell, Survival strategies of bacteria in the natural environment, Microbiol. Rev. 51 (1987) 365–379.

[7] C. Höfler, J. Heckmann, A. Fritsch, P. Popp, S. Gebhard, G. Fritz, T. Mascher, Cannibalism stress response in Bacillus subtilis, Microbiology 162 (2016) 164–176, https://doi.org/10.1099/mic.0.000176.

[8] E. Denkhaus, S. Meisen, U. Telgheder, J. Wingender, Chemical and physical methods for characterisation of biofilms, Microchim. Acta 158 (2007) 1–27, https://doi.org/10.1007/s00604-006-0688-5.

[9] J. Azeredo, N.F. Azevedo, R. Briandet, N. Cerca, T. Coenye, A.R. Costa, M. Desvaux, G. Di Bonaventura, M. Hébraud, Z. Jaglic, M. Kačániová, S. Knøchel, A. Lourenço, F. Mergulhão, R.L. Meyer, G. Nychas, M. Simões, O. Tresse, C. Sternberg, Critical review on biofilm methods, Crit. Rev. Microbiol. 43 (2017) 313–351, https://doi.org/10.1080/1040841X.2016.1208146.

[10] R. Valladares Linares, L. Fortunato, N.M. Farhat, S.S. Bucs, M. Staal, E. O. Fridjonsson, M.L. Johns, J.S. Vrouwenvelder, T. Leiknes, Mini-review: novel non-destructive in situ biofilm characterization techniques in membrane systems, Desalination Water Treat. 57 (2016) 22894–22901, https://doi.org/10.1080/19443994.2016.1180483.

[11] Y. Chao, T. Zhang, Surface-enhanced Raman scattering (SERS) revealing chemical variation during biofilm formation: from initial attachment to mature biofilm, Anal. Bioanal. Chem. 404 (2012) 1465–1475, https://doi.org/10.1007/s00216-012-6225-y.

[12] P. Stenclova, S. Freisinger, H. Barth, A. Kromka, B. Mizaikoff, Cyclic changes in the amide bands within Escherichia coli biofilms monitored using real-time infrared attenuated total reflection spectroscopy (IR-ATR), Appl. Spectrosc. 73 (2019) 424–432, https://doi.org/10.1177/0003702819829081.

[13] F. Humbert, F. Quilès, A. Delille, In situ assessment of drinking water biostability using nascent reference biofilm ATR-FTIR fingerprint, in: Current Research Topics in Applied Microbiology and Microbial Biotechnology, World Scientific, 2009, pp. 268–272, https://doi.org/10.1142/9789812837554_0056.

[14] M.C. Sportelli, S. Scarabino, R.A. Picca, N. Cioffi, Recent trends in the electrochemical synthesis of zinc oxide nano-colloids, in: CRC Concise Encyclopedia of Nanotechnology, 2015, pp. 1158–1172.

[15] M.C. Sportelli, R.A. Picca, N. Cioffi, Nano-antimicrobials based on metals, in: Novel Antimicrobial Agents and Strategies, Wiley-VCH Verlag GmbH & Co. KGaA, Weinheim, Germany, 2014, pp. 181–218, https://doi.org/10.1002/9783527676132.ch8.

[16] M. Sportelli, M. Valentini, R. Picca, A. Milella, A. Nacci, A. Valentini, N. Cioffi, New insights in the ion beam sputtering deposition of ZnO-fluoropolymer nanocomposites, Appl. Sci. 8 (2018) 77, https://doi.org/10.3390/app8010077.

[17] M.C. Sportelli, R.A. Picca, N. Cioffi, Recent advances in the synthesis and characterization of nano-antimicrobials, TrAC Trends Anal. Chem. (Reference Ed.) 84 (2016) 131–138, https://doi.org/10.1016/j.trac.2016.05.002.

[18] F. Quaranta, A. Valentini, P. Favia, R. Lamendola, R. D'Agostino, Ion-beam sputtering deposition of fluoropolymer thin films, Appl. Phys. Lett. 63 (1993) 10–11, https://doi.org/10.1063/1.109729.

[19] M.C. Sportelli, M.A. Nitti, M. Valentini, R.A. Picca, E. Bonerba, L. Sabbatini, G. Tantillo, N. Cioffi, A. Valentini, Ion beam sputtering deposition and characterization of ZnO-fluoropolymer nano-antimicrobials, Sci. Adv. Mater. 6 (2014) 1019–1025, https://doi.org/10.1166/sam.2014.1852.

[20] M.C. Sportelli, E. Tütüncü, R.A. Picca, M. Valentini, A. Valentini, C. Kranz, B. Mizaikoff, H. Barth, N. Cioffi, Inhibiting P. fluorescens biofilms with fluoropolymer-embedded silver nanoparticles: an in-situ spectroscopic study, Sci. Rep. 7 (2017), 11870, https://doi.org/10.1038/s41598-017-12088-x.

[21] N. Durán, M. Durán, M.B. de Jesus, A.B. Seabra, W.J. Fávaro, G. Nakazato, Silver nanoparticles: a new view on mechanistic aspects on antimicrobial activity, Nanomed. Nanotechnol. Biol. Med. 12 (2016) 789–799, https://doi.org/10.1016/j.nano.2015.11.016.

[22] A.J. Bard, M.V. Mirkin, Scanning Electrochemical Microscopy, second ed., CRC Press, 2012.

[23] G. Caniglia, C. Kranz, Scanning electrochemical microscopy and its potential for studying biofilms and antimicrobial coatings, Anal. Bioanal. Chem. 412 (2020) 6133–6148, https://doi.org/10.1007/s00216-020-02782-7.

[24] P. Sun, M.V. Mirkin, Kinetics of electron-transfer reactions at nanoelectrodes, Anal. Chem. 78 (2006) 6526–6534, https://doi.org/10.1021/ac060924q.

[25] C. Cai, B. Liu, M.V. Mirkin, H.A. Frank, J.F. Rusling, Scanning electrochemical microscopy of living cells. 3. Rhodobacter s phaeroides, Anal. Chem. 74 (2002) 114–119, https://doi.org/10.1021/ac010945e.

[26] D. Rudolph, D. Bates, T.J. DiChristina, B. Mizaikoff, C. Kranz, Detection of metal-reducing enzyme complexes by scanning electrochemical microscopy, Electroanalysis 28 (2016) 2459–2465, https://doi.org/10.1002/elan.201600333.

[27] A.A. Karyakin, E.E. Karyakina, Electroanalytical applications of prussian blue and its analogs, Russ. Chem. Bull. 50 (2001) 1811–1817, https://doi.org/10.1023/A:1014373811238.
[28] D. Battistel, F. Baldi, M. Gallo, C. Faleri, S. Daniele, Characterisation of biosynthesised silver nanoparticles by scanning electrochemical microscopy (SECM) and voltammetry, Talanta 132 (2015) 294–300, https://doi.org/10.1016/j.talanta.2014.09.023.
[29] G. Pecchielan, D. Battistel, S. Daniele, Scanning electrochemical microscopy and voltammetric investigation of silver nanoparticles embedded within a nafion membrane, Chemelectrochem 3 (2016) 2297–2304, https://doi.org/10.1002/celc.201600483.
[30] K.B. Holt, A.J. Bard, Interaction of silver(I) ions with the respiratory chain of Escherichia coli : an electrochemical and scanning electrochemical microscopy study of the antimicrobial mechanism of micromolar Ag+, Biochemistry 44 (2005) 13214–13223, https://doi.org/10.1021/bi0508542.
[31] A. Rizzuti, M. Dassisti, P. Mastrorilli, M.C. Sportelli, N. Cioffi, R.A. Picca, E. Agostinelli, G. Varvaro, R. Caliandro, Shape-control by microwave-assisted hydrothermal method for the synthesis of magnetite nanoparticles using organic additives, J. Nanoparticle Res. 17 (2015) 408, https://doi.org/10.1007/s11051-015-3213-0.
[32] M.C. Sportelli, M. Clemente, M. Izzi, A. Volpe, A. Ancona, R.A. Picca, G. Palazzo, N. Cioffi, Exceptionally stable silver nanoparticles synthesized by laser ablation in alcoholic organic solvent, Colloids Surf. A Physicochem. Eng. Asp. 559 (2018) 148–158, https://doi.org/10.1016/j.colsurfa.2018.09.046.
[33] R.F. Fan, D. Demaille, Preparation of tips for scanning electrochemical microscopy, in: A.J. Bard, M.V. Mirkin (Eds.), Scanning Electrochem. Microscopy, second ed., CRC Press, Boca Raton, 2012, pp. 25–51.
[34] F. Humbert, F. Quilès, in: A. Mendez-Vilas (Ed.), In-situ Study of Early Stages of Biofilm Formation under Different Environmental Stresses by ATR-FTIR Spectroscopy, Science against Microbial Pathogens: Communicating Current Research and Technological Advances, 2011, pp. 889–895.
[35] N. Cioffi, L. Colaianni, R. Pilolli, C.D. Calvano, F. Palmisano, P.G. Zambonin, Silver nanofractals: electrochemical synthesis, XPS characterization and application in LDI-MS, Anal. Bioanal. Chem. 394 (2009) 1375–1383, https://doi.org/10.1007/s00216-009-2820-y.
[36] V.K. Kaushik, XPS core level spectra and Auger parameters for some silver compounds, J. Electron. Spectrosc. Relat. Phenom. 56 (1991) 273–277, https://doi.org/10.1016/0368-2048(91)85008-H.
[37] A.V. Naumkin, K.-V. A, S.W. Gaarenstroom, C.J. Powell, NIST X-Ray Photoelectron Spectroscopy Database, 2012, https://doi.org/10.18434/T4T88K, Version 4.1.
[38] B. Abduali, T. Elmira, T. Ainur, Electrochemical behavior of silver in sodium sulphate solution during anodic polarization revisited, Orient. J. Chem. 29 (2013) 33–37, https://doi.org/10.13005/ojc/290105.
[39] S.S. Abd El Rehim, H.H. Hassan, M.A.M. Ibrahim, M.A. Amin, Electrochemical behaviour of a silver electrode in NaOH solutions, Monatshefte Fur Chemie 129 (1998) 1103–1117, https://doi.org/10.1007/PL00010123.
[40] N.A. Hampson, J.B. Lee, J.R. Morley, The electrochemistry of oxides of silver-a short review, Electrochim. Acta 16 (1971) 637–642, https://doi.org/10.1016/0013-4686(71)85174-5.
[41] S. Amemiya, A.J. Bard, F.-R.F. Fan, M.V. Mirkin, P.R. Unwin, Scanning electrochemical microscopy, Annu. Rev. Anal. Chem. 1 (2008) 95–131, https://doi.org/10.1146/annurev.anchem.1.031207.112938.
[42] M.L. Bruschi, Mathematical models of drug release, in: Strategies to Modify the Drug Release from Pharmaceutical Systems, Elsevier, 2015, pp. 63–86, https://doi.org/10.1016/B978-0-08-100092-2.00005-9.
[43] J. Siepmann, N.A. Peppas, Modeling of drug release from delivery systems based on hydroxypropyl methylcellulose (HPMC), Adv. Drug Deliv. Rev. 48 (2001) 139–157, https://doi.org/10.1016/S0169-409X(01)00112-0.
[44] A. El Afif, M. Grmela, Non-Fickian mass transport in polymers, J. Rheol. 46 (2002) 591–628, https://doi.org/10.1122/1.1470520.
[45] C. Radheshkumar, H. Münstedt, Antimicrobial polymers from polypropylene/silver composites-Ag+ release measured by anode stripping voltammetry, React. Funct. Polym. 66 (2006) 780–788, https://doi.org/10.1016/j.reactfunctpolym.2005.11.005.
[46] C. Damm, H. Münstedt, Kinetic aspects of the silver ion release from antimicrobial polyamide/silver nanocomposites, Appl. Phys. Mater. Sci. Process 91 (2008) 479–486, https://doi.org/10.1007/s00339-008-4434-1.
[47] M.H. Kim, T.-H. Kim, J.A. Ko, S. Ko, J.-M. Oh, H.J. Park, Kinetic and thermodynamic studies of silver migration from nanocomposites, J. Food Eng. 243 (2019) 1–8, https://doi.org/10.1016/j.jfoodeng.2018.08.028.
[48] G. Marletta, Chemical reactions and physical property modifications induced by keV ion beams in polymers, Nucl. Instrum. Methods Phys. Res. Sect. B Beam Interact. Mater. Atoms 46 (1990) 295–305, https://doi.org/10.1016/0168-583X(90)90716-8.
[49] L. Calcagno, G. Compagnini, G. Foti, Structural modification of polymer films by ion irradiation, Nucl. Instrum. Methods Phys. Res. Sect. B Beam Interact. Mater. Atoms 65 (1992) IN7–422, https://doi.org/10.1016/0168-583X(92)95077-5.
[50] A. Kondyurin, M. Bilek, 3 - interactions of energetic ions with polymers: chemical picture, in: A. Kondyurin, M. Bilek (Eds.), Ion Beam Treatment of Polymers, second ed., Elsevier, Oxford, 2015, pp. 29–67, https://doi.org/10.1016/B978-0-08-099445-1.00003-1. Second Edi.
[51] A. Kondyurin, M. Bilek, 4 - structure of polymers after ion beam treatment, in: A. Kondyurin, M. Bilek (Eds.), Ion Beam Treatment of Polymers, second ed., Elsevier, Oxford, 2015, pp. 69–127, https://doi.org/10.1016/B978-0-08-099445-1.00004-3. Second Edi.
[52] J.J. Dynes, J.R. Lawrence, D.R. Korber, G.D.W. Swerhone, G.G. Leppard, A. P. Hitchcock, Morphological and biochemical changes in Pseudomonas fluorescens biofilms induced by sub-inhibitory exposure to antimicrobial agents, Can. J. Microbiol. 55 (2009) 163–178, https://doi.org/10.1139/W08-109.
[53] E. Cefalì, S. Patanè, A. Arena, G. Saitta, S. Guglielmino, S. Cappello, M. Nicolò, M. Allegrini, Morphologic variations in bacteria under stress conditions: near-field optical studies, Scanning 24 (2002) 274–283, https://doi.org/10.1002/sca.4950240601.
[54] M.C. Sportelli, C. Kranz, B. Mizaikoff, N. Cioffi, Recent advances on the spectroscopic characterization of microbial biofilms: a critical review, Anal. Chim. Acta 1195 (2022), 339433, https://doi.org/10.1016/j.aca.2022.339433.
[55] A. Delille, F. Quilès, F. Humbert, In situ monitoring of the nascent Pseudomonas fluorescens biofilm response to variations in the dissolved organic carbon level in low-nutrient water by attenuated total reflectance-fourier transform infrared spectroscopy, Appl. Environ. Microbiol. 73 (2007) 5782–5788, https://doi.org/10.1128/AEM.00838-07.
[56] M. Kostakioti, M. Hadjifrangiskou, S.J. Hultgren, Bacterial biofilms: development, dispersal, and therapeutic strategies in the dawn of the postantibiotic era, Cold Spring Harbor Perspectives in Medicine 3 (2013), https://doi.org/10.1101/cshperspect.a010306 a010306–a010306.
[57] A. Fahs, F. Quilès, D. Jamal, F. Humbert, G. Francius, In situ analysis of bacterial extracellular polymeric substances from a Pseudomonas fluorescens biofilm by combined vibrational and single molecule force spectroscopies, J. Phys. Chem. B 118 (2014) 6702–6713, https://doi.org/10.1021/jp5030872.